Available online at www.sciencedirect.com
ScienceDirect
Journal of Catalysis 251 (2007) 485–496
JOURNAL OF CATALYSIS
www.elsevier.com/locate/jcat

Hydrogenation of tetralin on silica–alumina-supported Pt catalysts I. Physicochemical characterization of the catalytic materials

M.F. Williams [a], B. Fonfé [a], C. Sievers [a], A. Abraham [b], J.A. van Bokhoven [b], A. Jentys [a], J.A.R. van Veen [c], J.A. Lercher [a,*]

[a] *TUM, Institute for Chemical Technology 2, Lichtenbergstrasse 4, D-85747 Garching, Germany*
[b] *ETH Zurich, Institute for Chemical and Bioengineering, 8093 Zurich, Switzerland*
[c] *Shell International Chemicals B.V., Badhuisweg 3, 1031 CM Amsterdam, The Netherlands*

Received 5 March 2007; revised 2 June 2007; accepted 8 June 2007

Available online 18 September 2007

Abstract

A series of well-defined catalysts based on platinum nanoparticles supported on amorphous silica–alumina with varying composition was prepared by incipient wetness impregnation. Quantitative structural characterization of alumina and aluminosilicate domains by ^{27}Al (3Q) MAS NMR spectroscopy showed that the concentration of Brønsted acid sites determined by pyridine adsorption is related solely to the concentration of the aluminosilicate domain. However, only a very small fraction of the tetrahedrally coordinated aluminum led to the formation of Brønsted acid sites, because the negative charge on most of the tetrahedral Al–O was balanced by cationic aluminum oxide clusters. The preparation method led to small, uniform (0.6–0.8 nm) Pt particles on all aluminum-containing supports.

Keywords: Platinum; Catalysts; Nanoparticles; Amorphous silica–alumina; ^{27}Al 3Q MAS NMR; ^{1}H MAS NMR; Pyridine adsorption; EXAFS

1. Introduction

The interest in the acidic properties of amorphous silica–alumina (ASA) originates in their use in large-scale industrial catalytic processes [1,2]. ASAs have been used as catalysts or catalyst supports for such reactions as isomerization, alkylation of aromatic molecules, oligomerization of olefins, and cracking. Similar to zeolites, ASAs increase the resistance of a supported metal against sulfur poisoning in deep hydrotreating of diesel fuels [3,4]. However, due to their larger pores, ASA-based materials allow the conversion of significantly larger molecules than zeolite-based materials. The former materials have also a higher concentration of moderately strong but a lower concentration of strong Brønsted acid sites compared with zeolites. In this context, it should be noted that strongly acidic supports can lead to excessive coking and overcracking.

It has been reported that the properties of the support (i.e., chemical composition and the type, strength, and concentration of acid sites) influence the catalytic activity of platinum catalysts. However, the physicochemical properties of the catalysts studied varied in a wide range, and no systematic study of Pt/ASA catalysts has shown small Pt particles within a narrow size distribution and a gradual change in the acidic composition of the ASA supports. This is necessary to correlate acidity, metal–support interactions, and catalytic activity in the hydrogenation of aromatics in the presence of sulfur and nitrogen poisons for determining the different roles of the material properties in this set of complex reactions.

Here we report a comprehensive characterization of alumina-, ASA-, and silica-supported Pt catalysts with a view toward elucidating the structural origin of the acid sites in amorphous ASA supports. To directly probe the local configuration of the metal cations, we performed a solid-state magic angle spinning (MAS) NMR study. For aluminosilicates (e.g., ASA, zeolites), ^{27}Al NMR provides useful information on the Al–O environments, because chemical shifts depend strongly

* Corresponding author. Fax: +49 89 28913544.
E-mail address: johannes.lercher@ch.tum.de (J.A. Lercher).

0021-9517/$ – see front matter
doi:10.1016/j.jcat.2007.06.009

on the coordination number of aluminum [5–7]. Insight into the flexibility of some of the aluminum atoms was gained from a study of ammonia-treated samples. The treatment with ammonia is able to transform octahedrally coordinated aluminum oxide species back to the tetrahedral coordination, as long as the octahedrally coordinated aluminum is still connected to the framework via an oxygen atom [8,9]. ^{1}H MAS NMR and IR spectroscopy have been used for quantitative determination of the acidic properties of the various hydroxyl groups [10,11]. In the present study, the size and properties of the Pt particles were explored using transmission electron microscopy (TEM), hydrogen chemisorption, and extended X-ray absorption fine structure (EXAFS) spectroscopy.

2. Experimental

2.1. Preparation and chemical composition of supported Pt catalysts

A series of Pt-based catalysts supported on silica–alumina (ASA 5/95, 20/80, and 55/45, containing 5, 20, and 55% of alumina in silica, respectively), as well as on pure alumina and silica, were prepared by incipient wetness impregnation. The ASA supports were produced from a gel formed at pH 7.5 by mixing acetic acid with $AlCl_3{\cdot}6H_2O$ in distilled water (pH 1.5) and sodium silicate with NH_4OH (pH 12). The gel was washed with a diluted solution of ammonium acetate to eliminate Na^+ cations, dried at 400 K, and calcined at 949 K for 2 h. The supports were impregnated with an aqueous solution of $Pt(NH_3)_4(OH)_2$ for 1 h, calcined at 573 K for 5 h, and reduced at 623 K in a flow of hydrogen for 2 h.

2.2. Atomic absorption spectroscopy

The chemical compositions of the carriers and the supported catalysts were determined by atomic absorption spectroscopy (AAS) using a UNICAM 939 spectrometer.

2.3. Specific surface area and porosity

The surface areas and pore diameters were calculated from nitrogen adsorption measurements carried out at 77.4 K using a PMI automated BET sorptometer. Before the measurements, the samples were outgassed at 523 K for 20 h. The surface areas and micropore and mesopore distributions were calculated applying the BET and BJH theories.

2.4. Nuclear magnetic resonance spectroscopy

For the ^{27}Al (MQ) MAS NMR experiments, the catalyst samples were packed at ambient conditions into 4-mm ZrO_2 rotors. For further characterization of the octahedral aluminum species, the samples were heated in flowing NH_3 at 393 K for 6 h before being packed into the rotors.

The spectra were obtained by a Bruker Avance AMX 400 NMR spectrometer operating at 104.263 MHz for aluminum. MAS was carried out at a rotation rate of 12 kHz. The chemical shifts were referenced to solid $(NH_4)Al(SO_4)_2$ ($\delta_{Al} = -0.59$ ppm). For the MQ MAS NMR experiments, a three-pulse sequence, including z-filtering and state acquisition, was applied [12]. After Fourier transformation, the 2D spectra were sheared [13], so that the orthogonal projection on the isotropic axis gave the one-dimensional (1D) spectrum free of any anisotropic broadening. The quantification of different ^{27}Al species was performed by fitting the corresponding MAS spectra using the parameters determined in the 3Q MAS experiments [14]. The fitting was done using a program developed by the Kentgens group at the University of Nijmegen that uses Gaussian distributions for the quadrupolar coupling constant and the isotropic shift δ_{iso}.

^{1}H MAS NMR measurements were done using a Bruker AV 500 NMR spectrometer in a magnetic field of 11.7 T and at a spinning rate of 15 kHz. The prereduced dry samples (activated in vacuum for 1 h at 673 K) were pressed into 4-mm ZrO_2 rotors in dry nitrogen. The ^{1}H chemical shifts were referenced to the proton in the methine group of adamantane ($\delta = 2.0$ ppm).

2.5. Infrared spectroscopy

A Perkin–Elmer 2000 spectrometer operating at a resolution of 4 cm^{-1} was used in the IR studies. Before the IR investigation, the catalyst samples were activated in vacuum ($p = 10^{-6}$ mbar) at 673 K for 1 h. The activated catalyst samples were exposed to pyridine ($p_{(Py)} = 10^{-2}$ mbar) at 423 K for 0.5 h. After outgassing at 423 K for 1 h, the spectrum was recorded. Subsequently, the temperature was raised to 673 K and maintained at this temperature for 1 h. Then the sample was cooled to 423 K before the spectrum was recorded. The concentration of pyridine molecules retained on Brønsted and Lewis acid sites after outgassing at 673 K was defined as the concentration of strong acid sites. The difference between the concentrations of acid sites after outgassing at 423 and at 673 K is defined as the concentration of weak acid sites. The molar extinction coefficients published by Emeis were used for quantification [15].

2.6. Temperature-programmed desorption

The ca. 20-mg samples were activated in vacuum ($p = 10^{-3}$ mbar) by heating at 10 K min^{-1} to 673 K and maintaining that temperature for 1 h. After cooling to 423 K, the samples were exposed to pyridine for 1 h ($p_{(Py)} = 0.3$ mbar) and outgassed for another 3 h. Finally, the temperature was increased at a rate of 10 K min^{-1} while the desorption of pyridine was monitored by mass spectrometry using the $m/z^+ = 52$ signal. Overlapping desorption peaks were deconvoluted using Gaussian shapes to evaluate the desorption states [16]. Absolute concentrations were obtained from comparison with a standard (ZSM5, $SiO_2/Al_2O_3 = 180$ from Süd-Chemie, 0.19 mmol acid sites g^{-1}).

2.7. Transmission electron microscopy

The prereduced catalyst samples, stored under air, were ground, suspended in ethanol, and ultrasonically dispersed.

Drops of the dispersions were applied on a copper grid supported carbon film. A JEOL JEM-2010 transmission electron microscope operating at 120 kV was used.

2.8. H_2 chemisorption

The Pt catalysts were activated in vacuum at 588 K for 1 h to determine their H_2 chemisorption capacities. Subsequently, each sample was cooled to 298 K, after which successive doses of hydrogen were admitted. The amount of adsorbed hydrogen was determined by measuring the pressure after a time delay needed to reach the adsorption equilibrium. To account for the H_2 adsorbed on the support, the sample was outgassed and another isotherm was measured. The chemisorbed hydrogen on the metal was calculated by subtracting the second isotherm (i.e., hydrogen adsorbed on the support) from the first isotherm (i.e., hydrogen adsorbed on the metal and the support).

2.9. Extended X-ray absorption fine structure

The EXAFS spectra were collected at the beamline X1 at HASYLAB, DESY, Hamburg, Germany. The storage ring was operated at 4.5 GeV and an average current of 100 mA. The Si (311) double-crystal monochromator was detuned to 60% of the maximum intensity to minimize the intensity of higher harmonics in the X-ray beam. The fresh catalysts prepared as self-supporting wafers were reduced in situ by H_2 at 588 K for 2 h. The X-ray absorption spectra were collected at the Pt L_{III} edge (11,564 eV) at liquid N_2 temperature and further analyzed using Viper software [17]. For EXAFS analysis, the scattering contributions of the background were removed from the X-ray absorption by a third-order polynomial function. The oscillations were weighted with k^2 and Fourier-transformed within the limit $k = 3.5$–16 Å^{-1}. The local environment of the Pt atoms was determined from the EXAFS using the phase-shift and amplitude function for Pt–Pt, Pt–O, and Pt–Al calculated assuming multiple scattering processes (FEFF version 8.10) [18,19].

3. Results

3.1. Chemical composition and textural properties of the Pt catalysts

The chemical compositions of the Pt catalysts obtained in the AAS measurements are compiled in Table 1. The concentration of residual sodium cations was <33 μmol g^{-1} for all ASA supports. The platinum content was 1 wt% for Pt/SiO_2 and approximately 0.8 wt% for all other catalysts. The nitrogen adsorption–desorption isotherms of the catalyst samples were comparable to those of the parent materials. The ASA carriers had specific surface areas between 360 and 400 m^2 g^{-1}, higher than those of pure silica (64 m^2 g^{-1}) and alumina (310 m^2 g^{-1}).

Table 1
Chemical composition and textural properties of the calcined catalysts

Catalyst	Concentration (wt%)			BET surface area (m^2 g^{-1})	Pore diameter (nm)
	Pt	SiO_2	Al_2O_3		
Pt/Al_2O_3	0.78	0.0	99.2	307	8.7
Pt/ASA (55/45)	0.82	46.2	53.0	376	7.8
Pt/ASA (20/80)	0.81	78.8	20.4	363	9.4
Pt/ASA (5/95)	0.78	94.9	4.3	396	9.2
Pt/SiO_2	1.03	99.0	0.0	64	22

The chemical composition refers to water free catalysts.

3.2. Characterization of the aluminum species

^{27}Al 3Q MAS NMR spectroscopy was used to characterize the chemical environment of aluminum nuclei in the catalysts (Fig. 1). Quantitative analysis of the computed 1D ^{27}Al MAS NMR spectra was performed to obtain the concentrations of 4-, 5-, and 6-fold coordinated Al atoms using the quadrupolar and isotropic parameters derived from the 3Q MAS NMR spectra (Table 2). Additional information was obtained from treating the catalysts with ammonia before the NMR measurements. It was demonstrated that this treatment transforms some octahedrally coordinated aluminum species into tetrahedrally species, providing additional information on the state of octahedral Al species [8,9,20].

The ^{27}Al 3Q MAS NMR spectrum of Pt/Al_2O_3 showed signals at 66 and 7 ppm arising from tetrahedral (T) and octahedral (O) aluminum, respectively [21]. Each peak consists of a sharp component and a rather broad signal. The narrow resonance of T-Al is centered close to the diagonal, indicating that the corresponding aluminum species experiences a relatively small quadrupolar interaction (i.e., $\delta_{iso} \cong \delta_{F_2}$), pointing to a rather symmetric environment. The signal attributed to O-Al, stretched in the F_1 and F_2 dimensions, results from a large distribution in isotropic chemical shifts and quadrupolar interactions. This indicates a broad distribution of the electron density and the degree of distortion among the alumina–oxygen tetrahedra. The simulation of the 1D ^{27}Al MAS NMR spectrum required two contributions with different δ_{iso} and QCC parameters for both Al species (4- and 6-fold coordinated) to obtain a reasonable fit. The fractions of T and O aluminum were approximately 30 and 70%, respectively. The comparison with the 1D ^{27}Al MAS NMR spectrum of the ammonia-treated sample showed no significant changes in the position or the overall intensity of the peaks, indicating that little realumination occurred.

The resonance of T-Al was much stronger in the ^{27}Al 3Q MAS NMR spectrum of Pt/ASA (55/45) than in Pt/Al_2O_3. However, the signal was less well resolved, and its center shifted upfield to about 57 ppm. A new resonance at approximately 30 ppm was observed. In the literature, peaks at this position have been assigned to strongly distorted tetrahedral [14,22,23] or pentavalent aluminum species [24–27]. In the present case, the MQMAS spectrum contained a contribution at $\delta_{F_2} = 43$ ppm, which allows the unambiguous assignment of this resonance to 5-fold coordinated aluminum. The aluminum species in the octahedral environment were observed at 4 ppm. All peaks in the MQMAS spectrum of Pt/ASA (55/45) were broadened in the isotropic (F_2) and anisotropic (F_1) dimensions, suggesting that the topologic distributions of aluminum atoms in the amorphous sample and the bond angles are not well de-

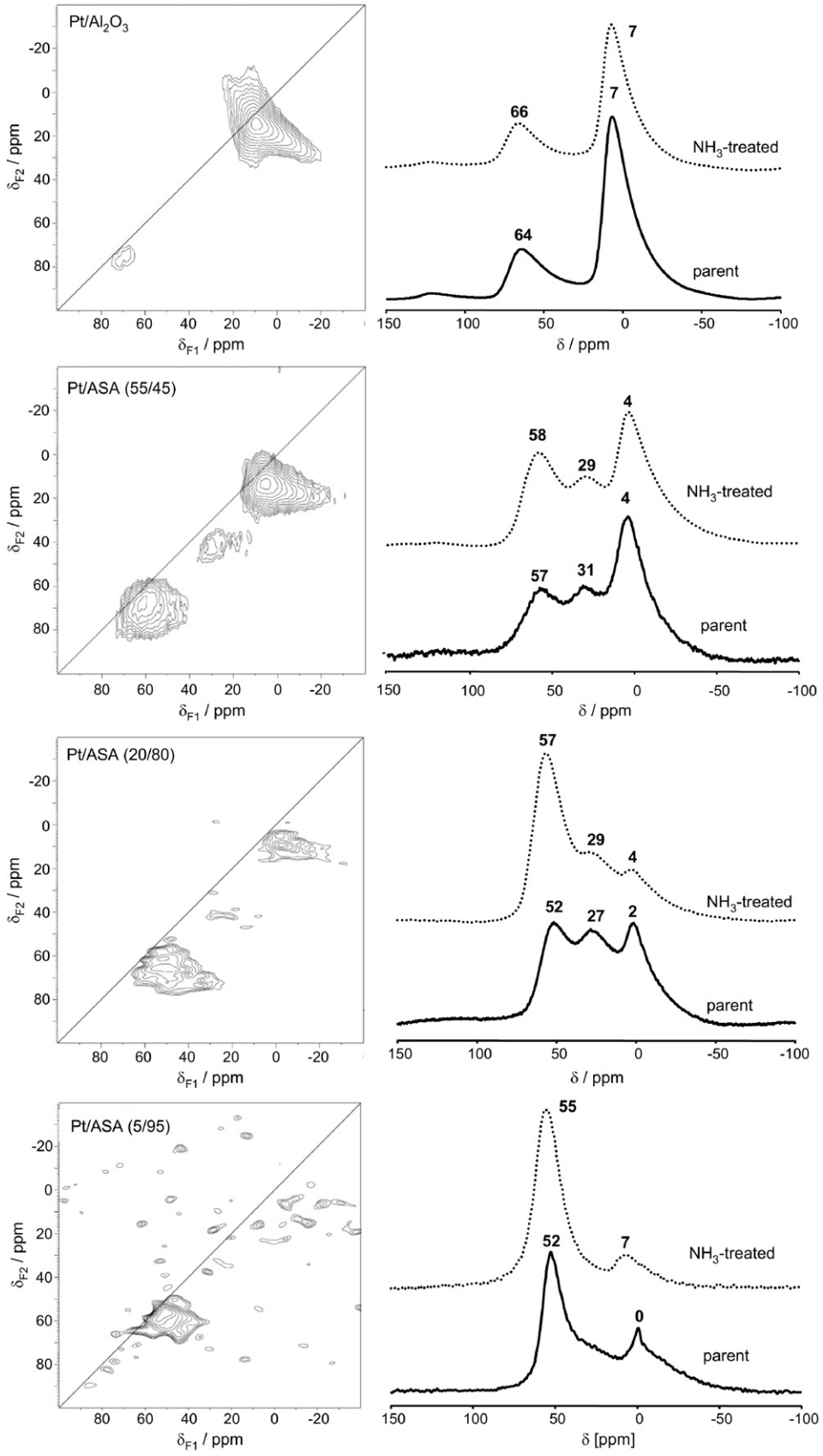

Fig. 1. ^{27}Al (MQ) MAS NMR study of Pt catalysts supported on alumina and ASAs. Left side: ^{27}Al 3Q MAS NMR spectra of the parent catalysts recorded at 104.263 MHz using a spinning rate of 12 kHz. Right side: Corresponding 1D ^{27}Al MAS NMR calculated on the basis of quadrupolar parameters derived from the 3Q MAS NMR data; the bottom spectrum represents that of the parent sample; the upper one corresponds to the catalyst sample treated with ammonia.

Table 2
Concentrations of different types of structural aluminum in alumina and in ASA supported Pt catalysts (in mol%)

Catalyst	Tetrahedral (T-Al)		Pentahedral (P-Al)		Octahedral (O-Al)	
	Parent	NH_3 treated	Parent	NH_3 treated	Parent	NH_3 treated
Pt/Al_2O_3	30	33	0	0	70	67
Pt/ASA (55/45)	25	34	26	26	49	40
Pt/ASA (20/80)	46	60	24	29	30	11
Pt/ASA (5/95)	69	87	0	0	31	13

fined. Whereas the T-Al signal was fitted with one value of QCC, both broad and sharp contributions were found for the O-Al species in the 1D spectrum. Ammonia treatment reduced the amount of O-Al (mainly the narrow QCC contribution) and increased that of T-Al by approximately 9% of the total Al concentration. This indicates that approximately 20% of the octahedrally coordinated aluminum atoms can be reinserted into the tetrahedral framework position (see Ref. [20] and references therein). Note that the intensity of the signal at 30 ppm did not change.

The NMR spectra of Pt/ASA (20/80) showed a remarkable upfield shift to 52 ppm of the peak attributed to T-Al, attributed to a significant dilution of aluminum in the neighborhood of a central Al atom. Some geometric factors (e.g., disordered Al–O–Si angles [28]) and the composition of the further coordination shells also could influence the resonance of T-Al [29]. The other aluminum species were found in 6- and 5-fold coordination states (resonance signals at 2 and 27 ppm, respectively). The relative concentration of T-Al was higher than that of the O-Al (46 vs 30%).

On ammonia adsorption, the intensity of the signal attributed to tetrahedrally coordinated aluminum increased significantly while, in parallel, the peak corresponding to octahedrally coordinated aluminum decreased. Note that the narrow feature in the octahedral region disappeared entirely, whereas only small changes were observed for the broad contribution. In addition, the T-Al peak was shifted slightly downfield to 57 ppm. Minor changes in the peak of the 5-fold coordinated aluminum were observed.

The NMR spectra of Pt/ASA (5/95) showed a substantial contribution of the 4-fold coordinated aluminum (at 52 ppm) and only minor resonance signals of 5- and 6-fold coordinated aluminum, indicating that most of the aluminum atoms adopted a tetrahedral coordination. The ammonia-treated sample showed a further increase of the fraction of 4-fold coordinated aluminum to 87% at the expense of 6-fold coordinated Al. As for Pt/ASA (20/80) the changes are associated mainly with the narrow feature in the octahedral region.

3.3. Surface structure of the catalysts

The different OH groups in the Pt catalysts activated at 673 K were characterized by ^{1}H MAS NMR spectroscopy (see Fig. 2). Because a rather narrow range of chemical shifts was considered, deconvolution was necessary to show the contributions of various OH groups.

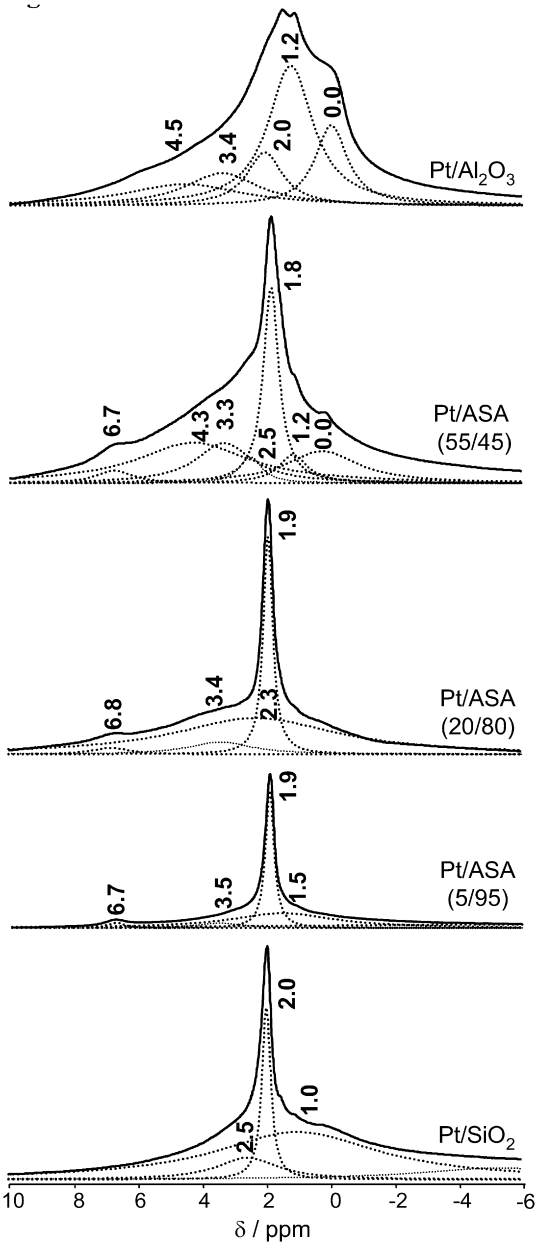

Fig. 2. ^{1}H MAS NMR spectra of Pt catalysts supported on alumina, ASAs and silica. Deconvolution with Lorentzian-shape peaks shows the contributions of various sorts of OH groups.

The ^{1}H MAS NMR spectrum of the Pt/Al_2O_3 catalyst showed several overlapping peaks at 0.0, 1.2, 2.0, 3.4, and 4.5 ppm. These result from the varying coordinations of the OH groups. The high-field signals at 0 and 1.2 ppm indicate a basic character of the hydroxyl group attached to a single aluminum atom. The signals at 2.0 and 3.4 ppm are assigned to bridging OH groups. Finally, the peak at 4.5 ppm is attributed to a mildly acidic OH group, which coordinates to three aluminum atoms [30].

The ^{1}H MAS NMR spectra of the Pt/ASA and Pt/SiO_2 exhibited a well-resolved peak at 1.8–2.0 ppm. The signal is assigned to Si–OH groups. The high-field component of every ASA spectrum was asymmetric due to some minor contribu-

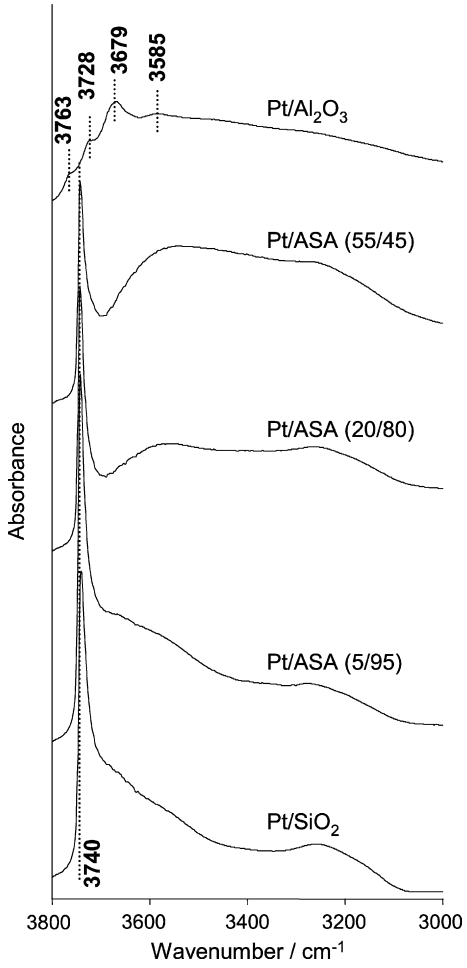

Fig. 3. IR spectra of activated Pt catalysts supported on alumina, ASA and silica.

tions that become less intense with decreasing concentration of alumina in the supports. In the ^{1}H MAS NMR spectrum of the Pt/SiO_2 catalyst, the Si–OH signal was asymmetric in the high-field region due to the presence of various types of silanol groups.

In contrast to the NMR spectra of Pt/Al_2O_3 and Pt/SiO_2 catalysts, the spectra of the ASA-supported samples always showed an additional signal at 6.7–6.8 ppm. Freude et al. [31, 32] assigned peaks at this position in the ^{1}H MAS NMR spectra of zeolites to small amounts of water adsorbed on Lewis acid sites. Alternatively, it was discussed that this resonance is due to the presence of structural OH groups compensating for the charge deficiency of Al–O tetrahedral in the mixed-oxide phase [33]. Note that none of the spectra showed a resonance of free bridging hydroxyl groups, which would be expected at ca. 4.0 ppm.

The corresponding IR spectra of the stretching vibration of OH groups are compiled in Fig. 3. For Pt/Al_2O_3, at least three major bands were detected at 3763, 3728, and 3679 cm^{-1}, assigned to OH groups bound to a single aluminum atom as well as to OH groups bridging two and three aluminum atoms [34]. The ASA- and silica-supported catalysts showed only one sharp band at 3740 cm^{-1}, attributed to terminal Si–OH groups. In addition, a broad band at lower wavenumbers, attributed to hydrogen-bonding OH groups, was observed in all samples. Note that these OH groups may be located in microcavities and thus are not necessarily accessible [35]. Free hydroxyl bands corresponding to Al-OH groups and bridging hydroxyl groups were not detected.

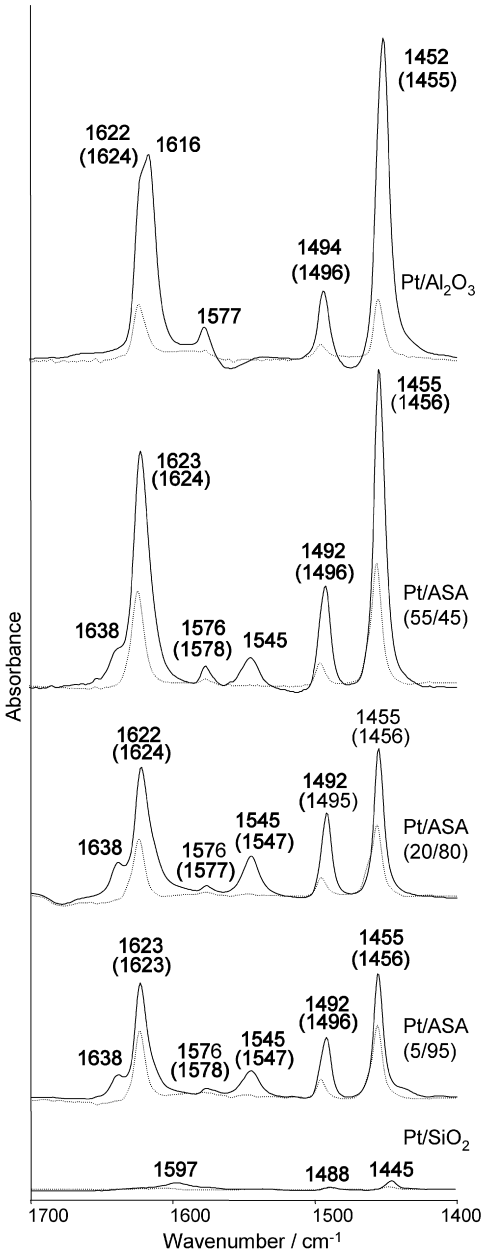

Fig. 4. IR spectra of pyridine adsorbed on alumina, ASA and silica supported Pt catalysts at $T = 423$ K, $p_{(Py)} = 2 \times 10^{-2}$ mbar (continuous lines). Spectra recorded upon temperature treatment (i.e., after outgassing at 673 K for 1 h) are also included (dashed lines, band values in brackets).

The acidic properties were characterized by pyridine adsorption/desorption followed by IR spectroscopy and TPD (see Figs. 4 and 5). With Pt/Al_2O_3, the IR spectrum of adsorbed pyridine (after evacuation at 423 K) showed bands at 1452, 1494, 1577, and 1616 cm^{-1} with a shoulder at 1622 cm^{-1}. These bands demonstrate that pyridine is solely coordinated

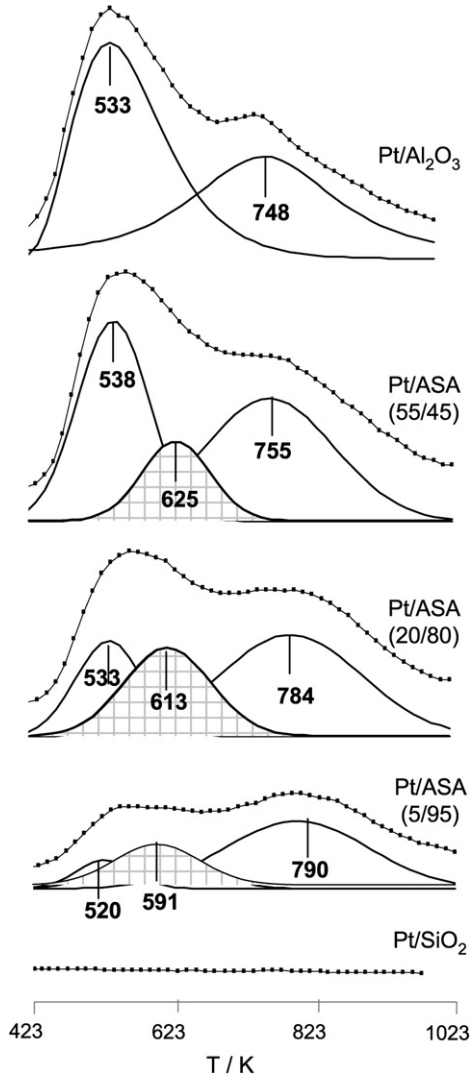

Fig. 5. TPD of pyridine adsorbed on alumina, ASA and silica supported Pt catalysts.

to Lewis acid sites. After evacuation at 673 K, bands were still observed at 1455, 1496, and 1624 cm^{-1}. In particular, the wavenumber of the first band indicates that alumina has very strong Lewis acid sites next to weaker ones characterized by the band at 1452 cm^{-1}.

Nearly identical bands were detected in the spectra of Pt/ASA samples, indicating the presence of pyridine adsorbed on Lewis acid sites (PyL species). Moreover, an additional band at 1545 cm^{-1} and a broad shoulder at 1638 cm^{-1} appeared, both of which are characteristic of pyridinium ions, indicating chemisorption of pyridine on Brønsted acid sites. After evacuation at 673 K, the intensity of all bands decreased. The peak at 1545 and the shoulder at 1638 cm^{-1} disappeared almost completely, demonstrating that the Brønsted acid sites were relatively weak.

With Pt/SiO_2, after pyridine adsorption and outgassing at 423 K, only three small peaks at 1445, 1488, and 1597 cm^{-1} were found, indicating weak adsorption via hydrogen bonding [36]. After outgassing at 673 K, the bands of adsorbed pyridine disappeared completely, indicating very weak sorption.

Table 3
Concentration of LAS and BAS calculated from Py-IR and Py-TPD

Catalyst	Conc. of LAS (mmol g^{-1})		Conc. of BAS (mmol g^{-1})		Conc. of strong LAS (mmol g^{-1})
	IR	TPD	IR	TPD	IR
Pt/Al_2O_3	0.14	0.13	0.00	0.00	0.02
Pt/ASA (55/45)	0.13	0.13	0.02	0.02	0.05
Pt/ASA (20/80)	0.09	0.09	0.04	0.04	0.05
Pt/ASA (5/95)	0.07	0.08	0.03	0.03	0.04
Pt/SiO_2	0.00	0.00	0.00	0.00	0.00

The rates of pyridine desorption during TPD (see Fig. 5) reveal the presence of two and three pyridine desorption peaks originating from Pt/Al_2O_3 and Pt/ASA catalysts, respectively. Pyridine adsorbed on Pt/SiO_2 did not lead to a detectable TPD trace, showing that pyridine was very weakly adsorbed on the sample and was desorbed after evacuation at 423 K.

In the case of the alumina-supported sample, the maximum desorption rate occurred at 533 and 748 K. Because Al_2O_3 exhibited only Lewis acidity, it can be concluded that these peaks correspond to desorption of pyridine from weak and strong Lewis acid sites. Silica–alumina supports showed similar low- and high-temperature desorption peaks at 520–538 and 755–790 K, respectively. The concentration of desorbing pyridine associated with the high-temperature desorption peak was similar for all of the samples. However, the relative strength of adsorption increased with decreasing alumina concentration, as indicated by a gradual shift in the maximum of the desorption peak temperature from 755 to 790 K. An additional medium temperature peak (maximum at approximately 610 K) was observed during desorption of pyridine from the ASA samples, attributed to desorption of pyridine from Brønsted acid sites.

Table 3 summarizes the quantification of the Lewis (LAS) and Brønsted (BAS) acid sites determined from TPD of pyridine and from quantitative evaluation of the IR spectra of adsorbed pyridine. It can be seen that both techniques show excellent agreement for the concentrations of the different types of acid sites (differences of $<10\%$). The concentration of Lewis acid sites was the highest for the Pt/Al_2O_3 catalyst and decreased in parallel to the concentration of alumina in the Pt/ASA samples. In contrast, Brønsted acidity was not observed for Pt/Al_2O_3 and passed through the maximum concentration of 0.036 mmol g^{-1} for Pt/ASA (20/80).

3.4. Characterization of supported platinum nanoclusters

The supported platinum particles were characterized by TEM, EXAFS and hydrogen chemisorption. A typical TEM image is shown in Fig. 6. The size histograms derived from the TEM micrographs for the alumina-, ASA-, and silica-supported Pt catalysts are compiled in Fig. 7.

For Pt on alumina and ASAs, the mean cluster size as determined by TEM was about 0.8 nm, with a standard deviation of 0.2 nm. The Pt/SiO_2 catalysts had larger metal particles (1.5 nm), with a standard deviation of 0.3 nm.

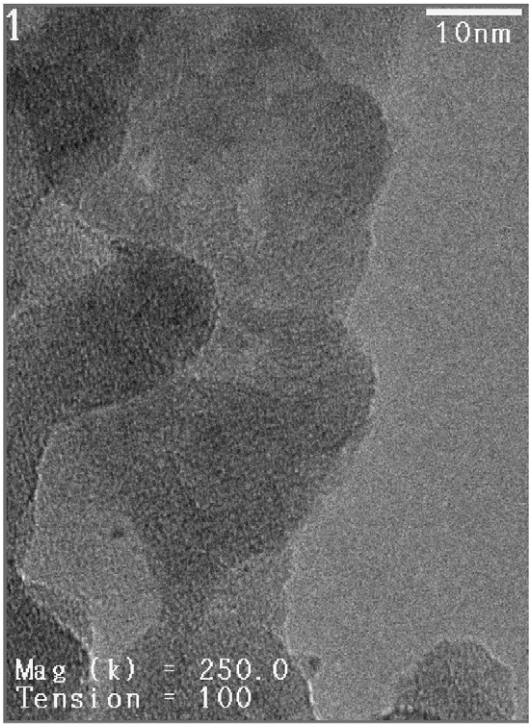

Fig. 6. TEM micrograph of Pt/ASA (5/95).

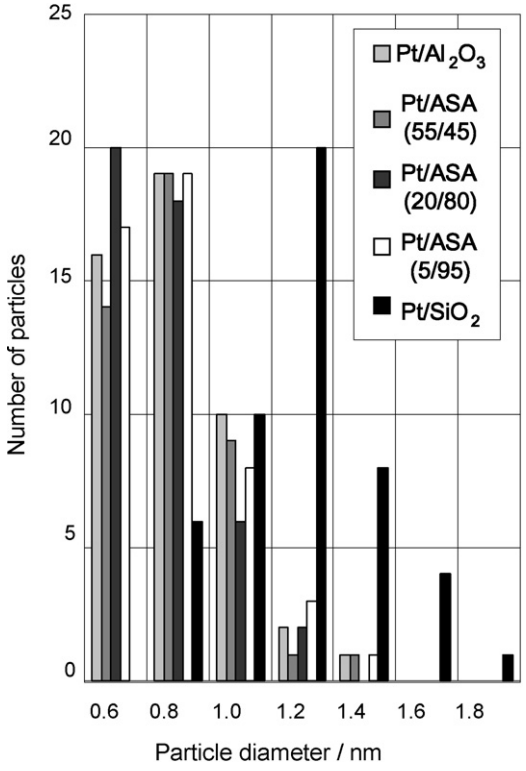

Fig. 7. Size histograms of alumina, ASA, and silica supported Pt catalysts.

The fraction of exposed metal was calculated from the irreversible hydrogen uptake at ambient conditions. The data indicate an H/Pt ratio of 0.94–1.00 for all samples except Pt/SiO_2, for which a value of 0.7 was determined. This indicates a smaller particle size for Pt on alumina and the ASA supports.

As a third method to determine the average particle size after reduction, EXAFS was used in combination with modeling the particle size using a cuboctahedral shape (see Fig. 8). The results of the EXAFS analysis of the reduced samples are compiled in Table 4.

The small particles of the Pt/ASAs are qualitatively visible from the low heights of the Pt–Pt first shell (N_1) contributions compared with bulk Pt. Pt/Al_2O_3, Pt/ASA (55/45), Pt/ASA (20/80), Pt/ASA (5/95), and Pt/SiO_2 showed contributions from the Pt–Pt coordinations at lesser distances compared with bulk Pt, and the coordination numbers for the Pt contributions in the first shell were between 4.0 and 7.6 (see Table 4). We speculate that the smaller interatomic distance of the Pt catalysts compared with bulk Pt is due to a stronger interaction between the atoms [37,38]. Assuming a cuboctahedral shape for the Pt particles, the average coordination number, metal dispersion, and particle size were estimated from the generic relations derived from models of the Pt particles [39]. The Pt particle sizes derived with this method were 0.6 nm for Pt/Al_2O_3, 0.8 nm for Pt/ASA (55/45), 0.7 nm for Pt/ASA (20/80), 0.8 nm for Pt/ASA (5/95), and 1.4 nm for Pt/SiO_2. A Pt–O contribution was observed in all oxide-supported Pt catalysts at around 2 Å. The coordination number of 1.4–1.9 between Pt and O provide further confirmation of the similar morphology for all ASA-supported Pt particles. The analysis of Pt–Al coordination showed no significant backscattering and thus were not included in the fits presented here.

4. Discussion

4.1. Domains in amorphous silica alumina and their implications for the acid site distribution

Conceptually, the ASA material may have three domains (i.e., silica, alumina, and a mixed-oxide phase) in which the aluminum cations substitute silicon cations in tetrahedral positions. The silica parts of ASA support are relatively uniform, terminating with hydroxyl groups that are at best mildly acidic. In addition to the hydroxyl groups, the alumina domains also exhibit Lewis acid sites resulting from coordinatively unsaturated aluminum cations in octahedral and tetrahedral position of alumina. In the mixed-oxide phase (i.e., the aluminosilicate phase) Brønsted acid sites also are formed by the isomorphous substitution of Si^{4+} by Al^{3+} ions. This leads to a negative charge on the aluminum-oxygen tetrahedron, requiring neutralization by cations. The relative fraction of the three phases depends on the chemical composition and the procedure for preparing the silica alumina material.

Because the material was amorphous, the separation into the domains had to be done through speciation of aluminum cations using ^{27}Al MAS NMR. In the first step, the aluminum species of the alumina phase were qualitatively and quantitatively characterized. In transition aluminas, the aluminum cations occurred in tetrahedral and octahedral coordination with oxygen. Within the restrictions imposed by the spinel lattice and the Al_2O_3 stoichiometry, the fraction of aluminum in tetrahedral coordination was between 25 and 37%. In the present case,

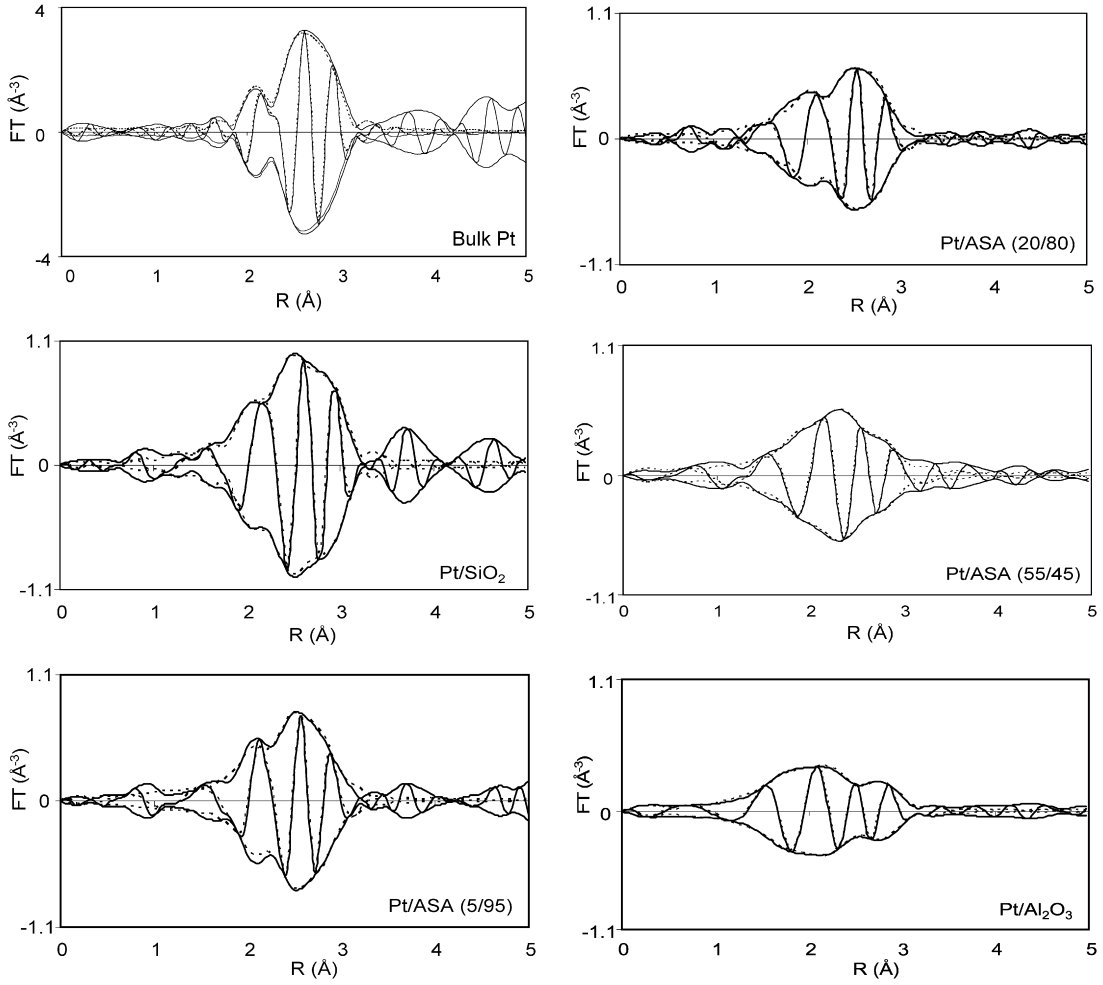

Fig. 8. Fourier transforms (k^2-weighted, Δk 3.5–16 Å^{-1}) of the Pt/ASAs and Pt foil (solid lines) and their Pt–Pt fitted contributions (dotted lines) after in situ H_2 reduction at 588 K.

Table 4
Results of the EXAFS analysis of the reduced Pt catalysts

Catalyst	Particle size[a] (nm)	H/Pt ratio[b]	Scatter	N	r (Å)	$10^3\Delta\sigma$[b] (Å^2)	ΔE_0 (eV)
Pt/Al_2O_3	0.8 (0.6–1.3)	0.97	Pt–Pt	4.0	2.64	9.0	8.3
			Pt–O	1.4	2.07	20.0	24.7
Pt/ASA (55/45)	0.8 (0.6–1.4)	1.00	Pt–Pt	5.7	2.65	9.0	0.3
			Pt–O	1.4	2.17	28.0	47.1
Pt/ASA (20/80)	0.75 (0.5–1.2)	0.94	Pt–Pt	4.7	2.68	8.0	10.6
			Pt–O	1.9	2.12	38.0	26.7
Pt/ASA (5/95)	0.8 (0.5–1.3)	1.00	Pt–Pt	6.2	2.71	8.0	9.8
			Pt–O	1.4	1.84	38.0	3.0
Pt/SiO_2	1.6 (0.8–2.2)	0.70	Pt–Pt	7.6	2.76	6.3	12.0
			Pt–O	1.2	2.01	30.0	21.5
Pt foil	–	–	Pt–Pt	12.0	2.76	3.4	11.1

[a] Determined by TEM measurement; minimum and maximum values are given in brackets.

[b] Determined by hydrogen chemisorption.

quantitative 1D ^{27}Al MAS NMR showed that 4-coordinated (tetrahedral) aluminum accounted for 30% of the total aluminum cations. The remainder were assigned to 6-fold coordinated (octahedral) aluminum cations. Treatment with ammonia did not transform octahedrally coordinated aluminum (O-Al) atoms into tetrahedrally coordinated aluminum (T-Al). Thus, the alumina phase did not contain a significant fraction of cations that could be reorganized by such treatment. Assuming that the alumina preserves the ratio of T-Al to O-Al, this will allow us to determine the relative fraction of the alumina domains if all of the other aluminum is reinserted into the mixed silica–alumina phase. Consequently, the aluminum on octahedral positions that can be reinserted and the pentacoordinated aluminum constitute the aluminum associated with the silica–alumina phase. Tetrahedrally coordinated aluminum in the silica–alumina phase is determined by the difference between the total concentration of the tetrahedrally coordinated aluminum and 3/7 of the concentration of the octahedrally coordinated aluminum that cannot be reinserted by the ammonia treatment.

The lower the aluminum concentration in the ASAs, the lower the likelihood of the formation of alumina domains. In parallel, insertion of alumina tetrahedra separated and surrounded by four silica tetrahedra is promoted (aluminosilicate phase). Using the chemical shift of 4-fold coordinated aluminum in the ^{27}Al MAS NMR spectra, it can be seen that most of the tetrahedral aluminum does not interact with neighboring Al atoms at a ca. 20% Al_2O_3 concentration in ASA. Note

Table 5
Distribution of the aluminum species in the Pt/ASA catalysts (in mmol g^{-1}, values in brackets in %)

Catalyst	Alumina patches		Amorphous silica–alumina phase			Total
	O-Al	T-Al	P-Al	O-Al	T-Al	
Pt/ASA (55/45)	4.84 (47)	2.25 (22)	2.66 (26)	0.29 (3)	0.35 (3)	10.39
Pt/ASA (20/80)	0.44 (11)	0.20 (5)	0.96 (24)	0.76 (19)	1.64 (41)	4.00
Pt/ASA (5/95)	0.11 (13)	0.05 (6)	0.00 (0)	0.15 (18)	0.53 (63)	0.84

that in the silica–alumina phase, the signal appeared at 52 ppm; compare this with the chemical shift of T-Al in pure alumina at 64 ppm. The octahedrally coordinated aluminum in ASA (20/80) can be almost completely converted to tetrahedrally coordinated aluminum on exposure to ammonia. Omegna et al. demonstrated that these aluminum nuclei must be present in the aluminosilicate phase so that they can be reintegrated into the tetrahedral coordination [20]. In contrast, aluminum species (which are not affected by this treatment) form a separate alumina phase. Therefore, this approach allows us to differentiate between aluminosilicate phases and pure alumina phases. Consequently, we conclude that only a very small fraction of an alumina phase existed in ASA (20/80). This contrasts strongly with the results for the ASA (5/95) and ASA (55/45) samples. In the latter case, only a small fraction of the octahedrally coordinated aluminum was converted to tetrahedrally coordinated aluminum after ammonia treatment. With ASA (5/95), changes and incorporation in the O-Al were observed, but a marked small peak at 10 ppm suggests that although this fraction of alumina had undergone changes, it remained octahedrally coordinated.

Several possible structures have been suggested for octahedrally coordinated aluminum species in zeolites that can be transformed into tetrahedrally coordinated ones. These suggestions include coordination to water molecules after partial hydrolysis of the framework [40] and a hydronium ion to a framework Al atom with a distorted tetrahedral coordination [8,9]. The second scenario is rather improbable in the present case, in which a considerable concentration of flexible aluminum and no indications of hydronium ions were found. Consequently, we conclude that partial hydrolysis in silica–alumina phases plays a major role in the formation of flexible aluminum. Due to the amorphous structure of ASA, it is not surprising that the concentration of flexible aluminum in this material exceeds that in zeolites [20].

The results demonstrate unequivocally that a perfect amorphous mixture of alumina and silica tetrahedra on the atomic scale does not form during the precipitation process [41]. Using the algorithm described above the contribution of alumina and silica–alumina domains can be estimated (see Table 5).

The MQMAS spectra showed that pentavalent Al was present in Pt/ASA (20/80) and Pt/ASA (55/45). Whereas the observation of pentavalent Al has been discussed in various publications [22–27], to date most studies have focused on proving or disproving its existence. Probably the most detailed

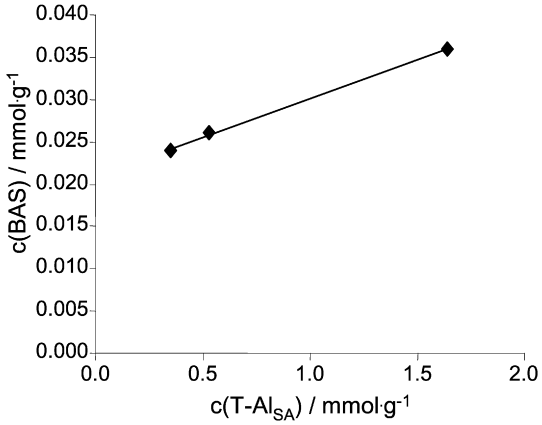

Fig. 9. Concentration of Brønsted acid sites (BAS) as a function of tetrahedrally coordinated aluminum in silica–alumina phases (T-Al_{SA}).

discussion has been given by De Witte et al. [24], suggesting that penta-coordinated aluminum is present as a highly disordered interface connecting an alumina domain with a silica or silica–alumina domain. Our measurements support this model. The concentration of pentavalent aluminum is significant only in aluminum-rich materials and does not vary with ammonia treatment, suggesting that the species is affiliated with the alumina phase. Because this is an interface phenomenon, the concentration of the species depends on the size and the concentration of the alumina domains.

4.2. *Formation of Brønsted acid sites in the ASA-supported platinum catalysts*

The silica–alumina domains contain two types of aluminum cations: surface-exposed O-Al with a flexible coordination environment and T-Al potentially generating Brønsted acid sites. For all ASA samples investigated, the concentration of Brønsted acid sites determined by IR spectroscopy and TPD of adsorbed pyridine were much lower than the concentration of T-Al. This suggests that a major fraction of the octahedrally coordinated aluminum in the ASA phase is used to compensate the negative charges of the oxygen aluminum tetrahedra in the silica–alumina phase. Fig. 9 shows that a linear correlation exists between the concentration of tetrahedrally coordinated alumina in silica–alumina phases (T-Al_{SA}) and the concentration of Brønsted acid sites. The offset on the y-axis indicates that at very low aluminum concentrations, a significantly higher fraction of the T-Al_{SA} atoms was able to form Brønsted acid sites. Note that the linear increase between the three samples corresponds to one Brønsted acid site per 100 T-Al_{SA} atoms.

In zeolites, Brønsted acidity is commonly attributed to the presence of bridging hydroxyl groups. In agreement with previous studies [20,27,42], the IR and NMR spectra of our samples did not provide direct evidence for the presence of these groups. However, IR spectroscopy clearly showed that the ASA-based samples contained a varying concentration of sites able to protonate pyridine. Crepeau et al. [27] suggested that these sites are silanol groups in the vicinity of tetrahedrally coordinated Al atoms. Trombetta et al. [42] proposed that Brønsted acid sites

are formed by the interaction of silanol groups with coordinatively unsaturated aluminum cations only in the presence of a base. However, even after activation, the samples in the present study contained small amounts of water adsorbed on strong Lewis acid sites. Although we do not want to rule out any of the models discussed above, we speculate that the molecular water adsorbed at an accessible (coordinatively unsaturated) tetrahedral aluminum was sufficiently polarized to protonate pyridine. Of course, this adduct was quite weak and decomposed well before the outgassing temperature of 400 °C at which the concentration of acid sites of higher strength was determined. This speculation is strongly supported by the presence of the signal at 6.7 ppm in the ^{1}H MAS NMR spectra of the ASA materials. Freude et al. [43,44] have attributed this peak to small amounts of water sorbed on Lewis acid sites of zeolites by the platinum phase in the ASA-supported platinum catalysts.

For very small Pt nanoclusters, the coordinatively unsaturated atoms from edges, corners, and surfaces represented a significant fraction of the Pt atoms, and, consequently, their average coordination number was smaller than that in the bulk metal. Hydrogen chemisorption provided a rough estimation of the number of these sites. TEM was needed to confirm information on the size distribution of metal clusters [45]. In addition, EXAFS analysis was used to study the very small metal particles in more detail. Thus, Pt–Pt coordination numbers were determined, and detailed information on the Pt cluster morphology became available by examining the Pt–O and Pt–Al contributions. The similar Pt–O coordination numbers of the Pt particles and the absence of significant Pt–Al backscattering in the present catalysts affirm a similar geometry of the Pt nanoclusters on all alumina-containing supports.

For the Pt/Al_2O_3, Pt/ASA (20/80), and Pt/SiO_2 catalysts, the particle sizes determined by TEM were slightly larger than those calculated from EXAFS. This discrepancy can be tentatively ascribed to the lower limit for the particle size, which can be detected by TEM. Nevertheless, there was very good correlation between the TEM and EXAFS data. Thus, overall, the metal particles were well distributed and uniform in size for all alumina-containing supports, providing a solid basis for evaluating the role of the support on the catalytic properties of Pt.

5. Conclusion

Amorphous silica–aluminas as supports for a series of Pt catalysts were characterized by various experimental techniques, focusing on the presence of different phases and domains in the amorphous material and the various types of acid sites. ASA supports can be synthesized with desired concentrations of silica, alumina, and aluminosilicate phases. Every phase contributed a different type of acidity. Weak and strong Lewis acid sites originated in the alumina clusters, whereas Brønsted acid sites were generated in the aluminosilicate phase. Four types of aluminum-containing species were identified: aluminum (tetrahedral and octahedral) in the form of a separate alumina phase, tetrahedral aluminum in the aluminosilicate phase, surface-exposed octahedral aluminum with flexible coordination connected to the aluminosilicate phase, and pentacoordinated aluminum connecting the alumina clusters within the silica/silica–alumina matrix.

The concentration of each type of aluminum was quantified by ^{27}Al MAS NMR. Up to 40% of the aluminum atoms in Pt/ASA (20/80) were incorporated into the aluminosilicate phase. Most of the resulting framework charges were compensated for by cationic aluminum species. Structural Brønsted acid bridging hydroxyl groups—as found in zeolites—were not detected in the IR and NMR spectra, despite the fact that a small number of sites capable of protonating pyridine were found. We assume that these may consist of water molecules adsorbed on Lewis acid sites. The Pt particles anchored by wet impregnation were small and uniform (0.6–0.8 nm) on all aluminum-containing supports.

Acknowledgments

Financial support was provided by SRTC Amsterdam. The authors thank the late Dr. W. Stork for critical discussions; Martin Neukamm and Xaver Hecht for the AAS and BET measurements, respectively. The XAFS experiments were carried out at station X1 at HASYLAB, DESY, Hamburg, Germany and supported by TMR Contract ERBFMGECT950059 of the European Community. Fruitful discussions in the framework of IDECAT are gratefully acknowledged.

References

[1] J. Scherzer, A.J. Gruia, Hydrocracking Science and Technology, Dekker, New York, 1996, chap. 12, p. 215.
[2] J. Ward, Fuel Process. Technol. 35 (1993) 55.
[3] J.A.R. van Veen, S.T. Sie, Fuel Process. Technol. 61 (1999) 1.
[4] W.R.A.M. Robinson, J.A.R. van Veen, V.H.J. de Beer, R.A. van Santen, Fuel Process. Technol. 61 (1999) 61.
[5] J. Klinowski, Prog. NMR Spectrosc. 16 (1984) 237.
[6] A.P.M. Kentgens, Geoderma 80 (1997) 271.
[7] D.D. Laws, H.-M.L. Bitter, A. Jerschow, Angew. Chem. Int. Ed. 41 (2002) 3096.
[8] J.A. van Bokhoven, D.C. Koningsberger, P. Kunkeler, H. van Bekkum, A.P.M. Kentgens, J. Am. Chem. Soc. 122 (2000) 12842.
[9] E. Bourgeat-Lami, P. Massiani, F. Di Renzo, P. Espiau, F. Fajula, Appl. Catal. A 72 (1991) 139.
[10] M. Hunger, D. Freude, H. Pfeifer, H. Bremer, M. Jynik, K.P. Wendlandt, Chem. Phys. Lett. 100 (1983) 29.
[11] D. Freude, Chem. Phys. Lett. 235 (1995) 69.
[12] J.P. Amoureux, C. Fernandez, S. Steuernagel, J. Magn. Reson. Ser. A 123 (1996) 116.
[13] R. Ernst, G. Bodenhausen, A. Wokaun, Principles of Nuclear Magnetic Resonance in One and Two Dimensions, Oxford Univ. Press, New York, 1987.
[14] J.A. van Bokhoven, A.L. Roest, D.C. Koningsberger, J.T. Miller, G.H. Nachtegaal, A.P.M. Kentgens, J. Phys. Chem. B 104 (2000) 6743.
[15] C.A. Emeis, J. Catal. 141 (1993) 347.
[16] GRAMS/32 Spectral Notebase Version 4.01 (1991–1996), Galactic Industries Corporation.
[17] K.V. Klementiev, VIPER for Windows, freeware: http://www.desy.de/~klmn/viper.html.
[18] A.L. Ankudinov, J.J. Rehr, Phys. Rev. B 62 (2000) 2437.
[19] A.L. Ankudinov, B. Ravel, J.J. Rehr, S.D. Conradson, Phys. Rev. B 58 (1998) 7565.
[20] A. Omegna, J.A. van Bokhoven, R. Prins, J. Phys. Chem. B 107 (2003) 8854.

[21] M.H. Lee, C.F. Cheng, V. Heine, J. Klinowski, Chem. Phys. Lett. 265 (1997) 673.
[22] M.P.J. Peeters, A.P.M. Kentgens, Solid State Nucl. Magn. Reson. 9 (1997) 203.
[23] S.M.C. Menezes, V.L. Camorim, Y.L. Lam, R.A.S. San Gil, A. Bailly, J.P. Amoureux, Appl. Catal. A 207 (2001) 367.
[24] B.M. De Witte, P.J. Grobet, J.B. Uytterhoeven, J. Phys. Chem. 99 (1995) 6961.
[25] J.P. Gilson, G.C. Edwards, A.W. Peters, K. Rajagopalan, R.F. Wormsbecher, T.G. Roberie, M.P. Shatlock, J. Chem. Soc. (1987) 91.
[26] G.J. Ray, A. Samoson, Zeolites 13 (1993) 410.
[27] G. Crepeau, V. Montouillout, A. Vimont, L. Mariey, T. Cseri, F. Mauge, J. Phys. Chem. B 110 (2006) 15172.
[28] H. Koller, E.L. Meijer, R.A. van Santen, Solid State Nucl. Magn. Reson. 9 (1997) 165.
[29] D. Freude, T. Fröhlich, H. Pfeifer, G. Scheeler, in: Second Workshop on the Adsorption of Hydrocarbons in Microporous Sorbents, Eberswalde, GDR, November 1982, vol. 2, p. 9.
[30] V.M. Mastikihin, I.L. Mudrakovsky, A.V. Nosov, Prog. NMR Spectrosc. 23 (Part 3) (1991) 259.
[31] D. Freude, H. Ernst, I. Wolf, Solid State Nucl. Magn. Reson. 3 (1994) 271.
[32] M. Hunger, D. Freude, H. Pfeifer, J. Chem. Soc. Faraday Trans. 87 (1991) 657.
[33] M. Hunger, D. Freude, H. Pfeifer, H. Bremer, M. Jynik, K.P. Wendlandt, Chem. Phys. Lett. 100 (1983) 29.
[34] X. Liu, R.E. Truitt, J. Am. Chem. Soc. 119 (1997) 9856.
[35] J.W. Geus, J.A.R. Van Veen, Catalysis: An Integrated Approach, Elsevier, The Netherlands, 1999, chap. 10, p. 459.
[36] T.R. Hughes, H.M. White, J. Phys. Chem. 71 (1967) 2192.
[37] B. Moraweck, G. Clugnet, A.J. Renouprez, Surf. Sci. 81 (1979) L631.
[38] B. Delley, D.E. Ellis, A.J. Freeman, E.J. Baerends, D. Post, Phys. Rev. B 27 (1983) 2132.
[39] Cerius 2 program suite, Accelrys Inc., 2001.
[40] G.L. Woolery, G.H. Kuehl, H.C. Timken, A.W. Chester, J.C. Vartuli, Zeolites 19 (1997) 288.
[41] Y. Kato, K. Shimizu, N. Matsushita, T. Yoshida, H. Yoshida, A. Satsuma, T. Hattori, Phys. Chem. Chem. Phys. 3 (2001) 1925.
[42] M. Trombetta, G. Busca, S. Rossini, V. Piccoli, U. Cornaro, A. Guercio, R. Catani, R.J. Willey, J. Catal. 179 (1998) 581.
[43] D. Freude, H. Ernst, I. Wolf, Solid State Nucl. Magn. Reson. 3 (1994) 271.
[44] M. Hunger, D. Freude, H. Pfeifer, J. Chem. Soc. Faraday Trans. 87 (1991) 657.
[45] K. Heinemann, F. Soria, Ultramicroscopy 20 (1986) 1.